



HAL
open science

Ice templating water-stable macroporous polysaccharide hydrogels to mimic plant stems

Katsuya Komiyama, Maya Allard, Corentin Eschenbrenner, Clémence Sicard, Ahmed Hamraoui, Francisco Fernandes

► **To cite this version:**

Katsuya Komiyama, Maya Allard, Corentin Eschenbrenner, Clémence Sicard, Ahmed Hamraoui, et al.. Ice templating water-stable macroporous polysaccharide hydrogels to mimic plant stems. *Journal of materials chemistry B*, 2025, 10.1039/D4TB02204A . hal-04928132

HAL Id: hal-04928132

<https://hal.science/hal-04928132v1>

Submitted on 4 Feb 2025

HAL is a multi-disciplinary open access archive for the deposit and dissemination of scientific research documents, whether they are published or not. The documents may come from teaching and research institutions in France or abroad, or from public or private research centers.

L'archive ouverte pluridisciplinaire **HAL**, est destinée au dépôt et à la diffusion de documents scientifiques de niveau recherche, publiés ou non, émanant des établissements d'enseignement et de recherche français ou étrangers, des laboratoires publics ou privés.



Distributed under a Creative Commons Attribution 4.0 International License

1 Ice templating water-stable macroporous
2 polysaccharide hydrogels to mimic plant stems

3

4 *Katsuya KOMIYAMA*¹, *Maya ALLARD*¹, *Corentin ESCHENBRENNER*¹, *Clémence SICARD*^{2,3},

5 *Ahmed HAMRAOUI*^{1,4}, *Francisco M. FERNANDES*^{1*}

6

7 ¹ Sorbonne Université, UMR 7574, Laboratoire de Chimie de la Matière Condensée de Paris, 75005,

8 Paris, France

9 ² Université de Versailles Saint-Quentin-en Yvelines, UMR 8180, L'Institut Lavoisier de Versailles,

10 78035, Versailles, France

11 ³ Institut Universitaire de France, Paris

12 ⁴ Université Paris Cité, CNRS, UMR8003, Saints Pères Paris Institute for the Neurosciences, 45, rue

13 des Saints-Pères, 75006 Paris, France

14

15 **Keywords;** alginate, cellulose nanocrystals (CNC), macroporous hydrogel, ice-
16 templating, capillary liquid transport

17

18 **Abstract**

19 Water-stable macroporous hydrogels, inspired by the structural and chemical

20 characteristics of plant stems are expected to open a wide range of possibilities in soft

21 materials for passive liquid transport. However, obtaining efficient materials for these

22 applications still poses a major challenge due to the complexity of shaping hydrogels at

23 the relevant scale-length. Here, water-stable macroporous hydrogels were fabricated

24 using alginate and TEMPO-oxidized cellulose via a new approach involving ice
25 templating and topotactic ion-crosslinking with Ca^{2+} . This approach allows to fully avoid
26 the energy-intensive lyophilization process and results in composite hydrogels with pore
27 sizes akin to those found in celery xylem, a model we chose for plant stems. Importantly,
28 the pore size could be tailored by adjusting both the ice-growth velocities and the ratios
29 of alginate to oxidized cellulose. The resulting hydrogels displayed remarkable water
30 stability along with viscoelastic properties and wettability that depend on the alginate and
31 oxidized cellulose ratios. Mechanical properties, such as compression stress and
32 toughness, consistently increased with higher alginate contents. In addition, liquid
33 transport measurements on crosslinked hydrogels with varying compositions and ice
34 growth velocities revealed comparable rising speeds to those observed in celery,
35 confirming the ability of polysaccharide-based hydrogels obtained by ice templating and
36 topotactic crosslinking as relevant materials to mimic the function of plant stems. Due to
37 their intrinsic biocompatibility, the materials presented here offer significant potential for
38 developing soft liquid transport systems suited for biological settings, with promising
39 applications in both environmental and bioengineering fields.

40

41 **1. Introduction**

42 In Nature, porous structures play a central role in large array of living organisms [1–4].
43 Some of the most striking examples come from plant stems, which feature highly
44 sophisticated porous architectures with a high degree of co-alignment. These porous
45 structures constitute the plants' vascular systems—the xylem and the phloem—that are
46 responsible for the capillary liquid transport of water and sap, respectively. Beyond the
47 fundamental understanding of liquid transport in natural materials, plants' vascular

48 systems are a major source of inspiration for a myriad of technological applications. In
49 particular, because of the role of the xylem network in plants, the capacity to mimic its
50 structure, its composition and its function is of technological interest in applications
51 where water transport regulation is required. In the literature, mimicking the xylem
52 network of plants has led to hydrogels with oriented porosity relevant in a broad range of
53 fields such as tissue engineering [5,6] and drug delivery [7,8]. Numerous fabrication
54 approaches such as micropatterning [9,10], 3D printing [11,12], oriented shear flow
55 [13,14], gravity-induced flow [15], electric field [16], and magnetic field [17] have been
56 proposed to obtain porous anisotropic hydrogels, but these rely on expensive equipment
57 and are applicable only to specific hydrogel compositions.

58 Recently, ice-templating (also known as freeze-casting or directional freezing) has gained
59 traction for its ability to create hydrogels with hierarchically aligned well-defined pores
60 in a straightforward and inexpensive process [18]. The technique relies on imposing a
61 controlled temperature gradient on a solution or suspension to induce solvent freezing
62 along a specific direction. Solutes, because they are mostly insoluble in ice [19,20], are
63 excluded from the ice fraction and accumulate together with any particle in suspension in
64 the interstitial space formed in between ice crystals. Upon removal of the ice crystals, the
65 process enables the formation of oriented porous materials whose characteristic size can
66 be adjusted by controlling the ice growth velocity. Here, we have implemented this
67 technique to elaborate materials featuring macroporous anisotropic features that mimic
68 the xylem network in plant stems.

69 Polysaccharides, mainly cellulose and hemicellulose, dominate the chemical composition
70 of plants and are of great interest due to their low toxicity, high biocompatibility, low cost
71 and high abundance. In this regard, mimicking plant structures using polysaccharides

72 exclusively would be an important step to design hydrogels that go beyond the structural
73 features of plant stems. However, only few reports have described the formation of water-
74 stable polysaccharide-based materials with ordered macroporous structure [21–23]. Such
75 limited examples are due to the abundant hydroxyl groups on the backbone of
76 polysaccharide chains. Most polysaccharides are either soluble in water (*eg.* chitosan,
77 alginate, starch, among others) or readily dispersible in aqueous environment (*eg.*
78 cellulose). This affinity towards water has dramatically reduced their potential use in the
79 context of materials for healthcare or environmental applications, where humid
80 environments prevail. To prevent these shortcomings, we have focused on two
81 polysaccharides that can be stabilized using a similar crosslinking strategy; alginate and
82 oxidized cellulose. Alginate is extracted from a family of brown algae. It is a linear,
83 unbranched polysaccharide consisting of 1,4-linked β -D-mannuronic acid and an α -L-
84 guluronic acid, which adopt random coil conformations in solution. Furthermore, in
85 presence of multivalent cations such as calcium—among others—ionic crosslinking
86 occurs, resulting in the formation of a hydrogel stabilized by “egg-box” structures (Figure
87 S1) [24]. Cellulose is composed of β -1-4-linked D-anhydroglucose units and is commonly
88 extracted from wood, hemp, cotton, etc. The reaction between cellulose and 2,2,6,6-
89 tetramethylpiperidine-1-oxyl radical (TEMPO) results in the selective oxidation of the
90 hydroxyl groups at the C₆ position on the cellulose surface and induces the formation of
91 carboxylate groups [25] (Figure S2). As with alginate, interaction of the carboxylate
92 groups of cellulose and cations results in stable hydrogels [26,27]. These interactions
93 stand as a key advantage to stabilize multicomponent hydrogels in a single step, leading
94 to increases stability in comparison to single component hydrogels, due to reinforcement
95 effects [28–30]. However, to date this crosslinking method has never been applied for the

96 design of water-stable ice-templated polysaccharide-based hydrogels without an
97 intermediate step requiring the energy-intensive process of lyophilization. The main
98 challenge lies in the need to remove the ice while promoting the stabilization of the freeze
99 concentrated phase. Traditionally this is obtained by lyophilization, where ice crystals are
100 sublimated to produce a dry foam of solutes. However, this approach fails in the case
101 where the solutes are water-soluble. To circumvent this limitation and thus the loss of the
102 macroporous structure, herein, we replaced lyophilization by topotactic stabilization. A
103 strategy our team developed for compositions containing type I collagen, that allows
104 transforming frozen monoliths of biopolymer solutions into macroporous hydrogels
105 without a drying step [31].

106 We applied this strategy to dispersions of cellulose nanocrystals (CNC), which are
107 longitudinal, crystalline nanoparticles derived from cellulose, in alginate solution to
108 mimic part of the complex architecture and composition of plants' stems. The materials
109 generated by this approach were water-stable and could be designed with pores (50-100
110 μm in diameter) that exhibit dimensional similarity to the xylem of celery (*Apium*
111 *graveolens*). The performance of the alginate-CNC ice templated hydrogel as water
112 transport devices were compared with decellularized celery. To untangle the impact of
113 the polysaccharide composition on the morphology, mechanical and water transport
114 properties, the ratio between alginate and oxidized cellulose in the precursor
115 solution/suspension was varied to its widest range. Finally, we demonstrate that the
116 capillary transport properties of alginate-oxidized cellulose hydrogels are mainly
117 dominated by the pore size, suggesting their potential utility in biomedical and
118 environmental applications with an easily tuned macroporosity.

119

120 **2. Material and Methods**

121 **2.1. Materials**

122 Sodium alginate and $\text{CaCl}_2 \cdot 2\text{H}_2\text{O}$ were purchased from Sigma-Aldrich and used without
123 further purification. Cellulose nanocrystals (CNC) with a sulfate content of 0.25 mmol/g
124 (determined by conductivity) were purchased from CelluForce (Canada) and oxidized
125 through TEMPO (2,2,6,6-tetramethylpiperidine-1-oxy radical)-mediated oxidation to
126 obtain oxidized cellulose [32]. Briefly, cellulose nanocrystals (10 g) were suspended in
127 water (1 L) containing TEMPO (0.156 g) and NaBr (2.572 g). A solution of NaClO (12
128 wt%) was added to the suspension under stirring and the mixture was kept at pH = 10
129 by adding 0.5 M NaOH. The reaction was quenched by adding methanol (1 mL) and the
130 pH of the mixture was lowered to 7 by adding 0.1 M HCl solution. The mixture was
131 dialyzed for 7 days (Spectra/Por[®] 4, SpectrumLabs). Finally, the suspension was
132 lyophilized to obtain dry oxidized cellulose powder. The carboxylate content of oxidized
133 cellulose was 0.76 mmol/g based on electrical conductivity titration.

134 **2.2. Plant stem decellularization**

135 Celery (*Apium graveolens*) were purchased at a local supermarket (Paris, France).
136 Decellularization of the celery stem was conducted according to the method reported by
137 Esmaeili *et al.* [33] (Figure S3). The stem was cut into 1 cm thick transversal sections,
138 immersed in 10% SDS solution, and placed in an orbital shaker at 180 rpm at 25 °C for 5
139 days. After decellularization, samples were washed with distilled water several times and
140 immersed in the solution containing 5 w/v% NaOCl and 3 w/v% NaOH at 25 °C for 1
141 day. Finally, samples were washed with distilled water several times and stored at 4°C
142 until further use.

143 **2.3. Fabrication of ion-crosslinked anisotropic hydrogels**

144 Macroporous hydrogels consisting of alginate and oxidized cellulose were prepared by
145 unidirectional ice-templating method followed by crosslinking with Ca^{2+} (Scheme 1).

146 The ice-templating setup was composed of a cold finger—a heat conductive aluminum
147 rod partially immersed in liquid nitrogen. Temperature profiles at the top of the cold
148 finger were controlled via a heating resistance controlled by a Proportional–integral–
149 derivative (PID) programmed to ensure a linear progression of the ice front [34].

150 Alginate-oxidized cellulose relative concentration was set to 7 different ratios with a fixed
151 total solute concentration of 40 g/L (A:C=8:0, 7:1, 6:2, 4:4, 2:6, 1:7 and 0:8, where A and
152 C stand for alginate and oxidized cellulose, respectively) The ratios are shown in Table
153 1.

154

155 **Table 1.** Composition of the macroporous polysaccharide samples.

Alginate:Oxidized Cellulose (A:C)	Alginate / g L⁻¹	Oxidized Cellulose / g L⁻¹
8:0	40	0
7:1	35	5
6:2	30	10
4:4	20	20
2:6	10	30
1:7	5	35
0:8	0	40

156

157 For each sample, 2 mL of the suspension were poured inside 12 mm diameter cylindrical
158 molds, placed at the top of the aluminum rod. The bottom of the suspension in the mold

159 was then cooled down from 20 to -80 °C. To explore the impact of the composition on
160 the properties of the obtained hydrogels we have fixed the ice front velocity at 25 μm/s.
161 Conversely, to assess the impact of the ice front velocity on the properties of the hydrogels,
162 we fixed the alginate/oxidized cellulose ratio (A:C=4:4) and applied three different ice-
163 front velocities (10 μm/s, 25 μm/s and 50 μm/s) (Figure S4).

164 After ice templating, all obtained suspensions were crosslinked in 1 M CaCl₂ solution for
165 24 hours. To ensure that topotactic crosslinking (melting of the ice crystals with
166 preservation of the porous structure) took place, samples were placed at -3 °C, above the
167 melting point of CaCl₂ solution but below the melting point of pure ice, resulting in self-
168 supported crosslinked hydrogels that do not disperse in the CaCl₂ solution [31].

169 **2.4. Morphology of the hydrogels**

170 The hydrogels and the stem of the celery were observed using SEM (S-3400N, Hitachi,
171 Japan) at an accelerating voltage of 10 kV. All samples were coated with a 10 nm layer
172 of gold before observation. After the Ca²⁺ crosslinking, the hydrogels were dehydrated in
173 successive ethanol baths (30, 50, 70, 80, 90, 95 and 100%) followed by supercritical CO₂
174 drying. When plunged into the ethanol bath, sample A:C=0:8 was rapidly dispersed,
175 preventing its observation by SEM. Images acquired using SEM for the rest of the
176 samples were analyzed with the MorpholibJ plugin [35] in FIJI software[36] to
177 investigate the pore size and distribution. Over 100 pores were counted per SEM image
178 to provide statistically representative values for the pore cross-section areas.

179 **2.5. Rheological characterization**

180 The viscosity of the precursor suspensions with different alginate/oxidized cellulose
181 ratios before crosslinking were determined using a rheometer (MCR 302, Anton Paar,
182 Austria). A 25 mm diameter cone-plate geometry with 1° angle was used. The viscosity

183 measurement was conducted by applying a growing shear-rate from 1 to 500 s⁻¹ at 25 °C.
184 The rheological measurements of the different precursor suspensions were carried out
185 after crosslinking with Ca²⁺ ions, using a MCR302 rheometer under a parallel-plate
186 configuration (diameter of 25 mm). The suspensions (1 mL) were introduced onto the
187 bottom plate and crosslinked with 1 mL of 1 M CaCl₂ solution 5 minutes before loading
188 the top plate. The frequency sweep was performed from 0.1 to 10 Hz with 1% amplitude
189 at 25 °C.

190 **2.6. Water stability test of ion-crosslinked hydrogels**

191 Water stability tests were carried out on all Ca²⁺-crosslinked hydrogels, from pure
192 alginate to pure oxidized cellulose. Each hydrogel was immersed in 20 mL of distilled
193 water and stored for 30 days at room temperature. The stability was assessed visually by
194 the sample deformation after this period.

195 **2.7. Mechanical properties of hydrogels**

196 Compression tests of the crosslinked hydrogels were carried out using a rheometer in
197 compression mode (MCR 302, Anton Paar, Austria). The compression speed was set to
198 1 mm/min and samples were compressed until 60% strain. Samples' dimensions were
199 about 12 mm in diameter and 10 mm in height. A total of 5 replicates were averaged for
200 each sample. Young's modulus was defined from the maximum slope in the low strain
201 regime (0 to 10%). Toughness was determined by the area under the stress-strain curves
202 until 60% stain.

203 **2.8. Wettability**

204 To characterize the wettability of the different crosslinked hydrogels, films with different
205 ratios of alginate and oxidized cellulose were prepared by casting the suspensions on
206 optical microscopy glass slides, with fixed height of 2 mm, using a doctor blade knife.

207 Subsequently, cast suspensions were crosslinked by dipping the slides into 1 M CaCl₂
208 solution at room temperature. The deposited films were peeled off the glass slides with
209 the exception of A:C=1:7 and 0:8 samples, which adhered strongly to the surface of the
210 glass slides and could not be removed. The contact angle formed between the film and
211 water was determined by assessing the interfacial force using the Wilhelmy plate method
212 [37]. During the measurement, a film was suspended from the sample holder, which was
213 connected to an automated microbalance, and partially immersed in distilled water.
214 Samples were then vertically pulled from, and then pushed into the water at room
215 temperature at a constant speed rate of 0.05 mm/s which results in both receding and
216 advancing contact angles, respectively. The dimensions of the films were 10×5×0.05 mm³.
217 The contact angles were determined in degrees using the following relation:

$$218 \quad \theta = \cos^{-1} \frac{F_w}{L\sigma} \quad (1)$$

219 where σ is the surface tension of water (mN·m⁻¹), F_w is the wetting force (mN), L is the
220 length of the triple phase line (defined by the film, the air and the water around the sample
221 section) (m) and θ is the contact angle (°).

222 **2.9. Liquid transport**

223 Crosslinked hydrogels with different compositions/ice-growth velocities were used for
224 the liquid transport measurements. Samples were fixed with 2 needles onto a home-built
225 sample holder brought to contact with a 200 ppm methylene blue (MB) solution (lifted
226 progressively by a lab jack until the liquid surface reached the bottom of the sample). The
227 progression of the methylene blue in the hydrogels was recorded with video camera (Q-
228 scope QS.20200-P) for 1 hour at 16 frames per second. The obtained video footage was
229 analyzed with FIJI software. The surface tension of the methylene blue solution used here
230 was 65 mN/m [38]. A control experiment was performed using single hydrogel walls

231 (prepared as described above by doctor blade casting followed by crosslinking for three
232 different compositions, 2:6, 4:4 and 6:2 A:C). The movement of the dye was monitored
233 as outlined earlier.

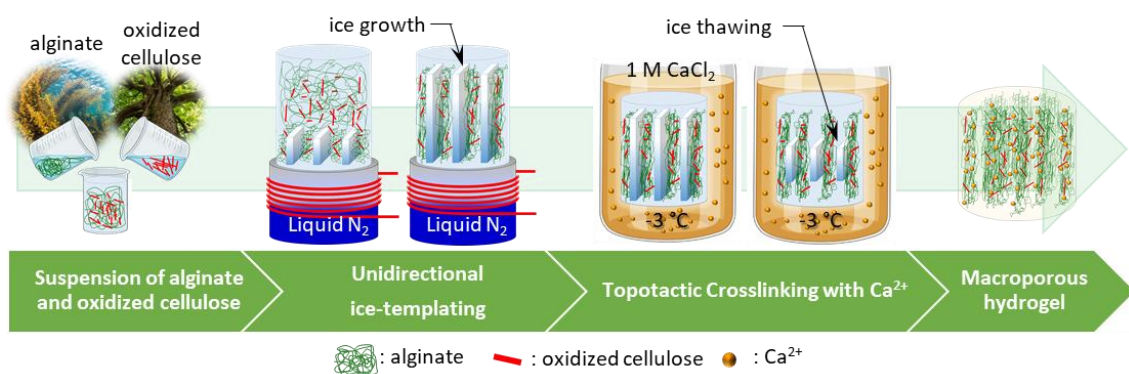
234

235 3. Results and discussion

236 3.1. Macroporous alginate-CNC gels obtained by ice templating and topotactic 237 crosslinking

238 Ice templating exploits the poor solubility of most solutes in ice, resulting in the formation
239 of two different phases during freezing. One phase is composed of pure ice, and the
240 second corresponds to freeze-concentrated solutes in between the ice crystals. To remove
241 the ice without altering the macroporous structure, here, we implemented topotactic
242 stabilization strategy [31]. This technique relies on the concomitant occurrence of ice
243 thawing and polymer crosslinking. Here, we have selected CaCl_2 at a concentration of 1
244 M to induce crosslinking of the alginate-CNC system (Scheme 1).

245



246

247 **Scheme 1.** Schematic illustration of the fabrication process of macroporous anisotropic hydrogels
248 consisting of alginate and oxidized cellulose.

249

250 Alginate and oxidized cellulose are crosslinked when exposed to Ca^{2+} ions, leading to the

251 formation of gels. In addition, the presence of CaCl_2 at this concentration induces a strong
252 cryoscopic depression (*ca.* -5°C). Together, these conditions ensure that, when a frozen
253 monolith is placed in a CaCl_2 solution, at a temperature between 0 and -5°C , the sample
254 can be progressively transformed into an unfrozen crosslinked hydrogel. We have applied
255 this strategy to the elaboration of macroporous alginate-CNC materials ranging from pure
256 alginate to pure CNC. Regardless of the composition, the resulting materials are fully
257 self-supported, as can be seen in the left-hand side images in Figure 1a-f. The longitudinal
258 sections of the samples, depicted in Figure S5 confirm the pores run parallel to the
259 temperature gradient applied during freezing, regardless of the studied compositions.
260 Notably, pure CNC hydrogel (A:C 0:8) was found unstable in ethanol solution impeding
261 its observation under SEM. While the changes in composition do not affect the
262 macroscopic stability nor the orientation of pores of the obtained hydrogels, SEM
263 observations of the transversal sections of these samples (Figure 1a-f) indicate that the
264 polysaccharide composition does play a major role in determining the pores' dimensions
265 and morphology.

266 Figure 1i depicts the pore area distribution (taken from the area of the pore in the
267 transversal cross-section). Samples exclusively composed of alginate (A:C=8:0) display
268 anisotropic pore section that tend to pack together producing co-alignment (Figure 1a).
269 Increasing the oxidized cellulose content produces larger pores (Figure 1i). The increase
270 in pore dimensions, resulting from increasing CNC content, also results in wider pore size
271 distribution (Figure S6a). In other words, alginate favors smaller and more homogeneous
272 pores with narrower size distribution, whereas CNC promotes bigger, more polydisperse
273 pores.

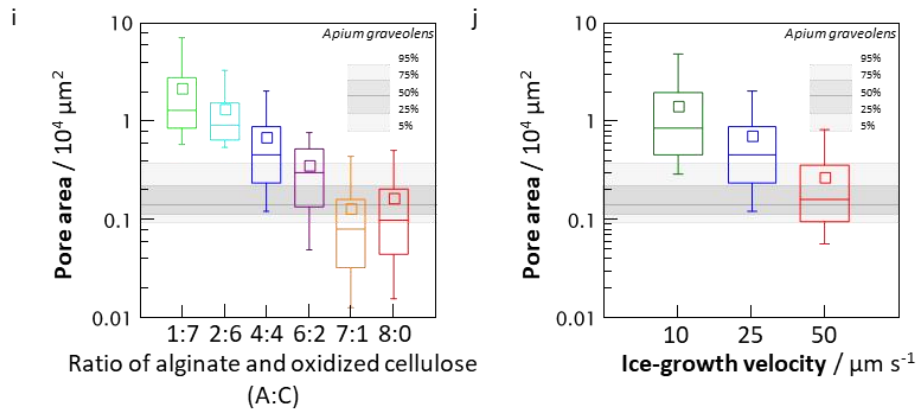
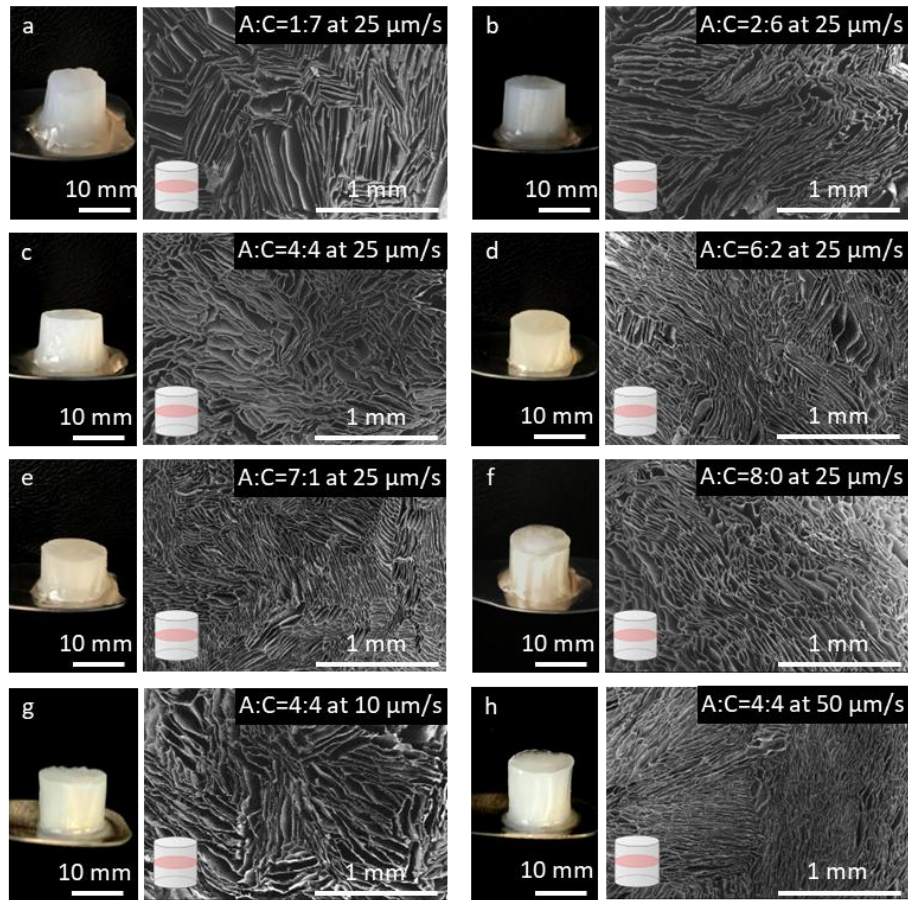
274 One of the key factors affecting the growth of ice crystals during ice-templating (and thus

275 determining the final dimensions of the pores in the final materials) is the viscosity of the
276 precursor solution/suspension. We investigated the viscosity of the different compositions
277 of alginate and oxidized cellulose to ascertain their impact on the pore size of mixed
278 polysaccharide hydrogels (Figure S7). The viscosity of the suspensions progressively
279 increased with the ratio of alginate, regardless of the shear rate. This could be associated
280 with the intrinsically low viscosity of oxidized cellulose nanocrystal rods and the
281 relatively high viscosity of entangled alginate chains. In addition, the viscosity of all
282 suspensions showed shear-thinning behavior, which was more pronounced for higher
283 ratios of alginate. This effect could be ascribed to the disentanglement of alginate chain
284 coils under shear [39], even if strong shear thinning effects have equally been reported
285 for CNCs [40].

286 The viscosity values determined for the different aqueous suspensions of polysaccharides
287 display an inverse relationship with the pore size. This observation confirms the strong
288 dependence between porosity and viscosity widely discussed in the literature for other
289 compositions [41]. Here, high alginate fractions impose higher viscosity to the
290 polysaccharide solutions/suspension, resulting in restricted lateral growth of ice crystals
291 and consequently smaller and more uniform pore size for the same ice front velocity [42].
292 However, ascribing the differences in pore size exclusively to the viscosity implies that
293 the different polysaccharides do not have specific interactions with ice during the freezing
294 events.

295 SEM images in the transversal section of the hydrogels prepared at 4:4 ratio of alginate
296 and oxidized cellulose with different ice-growth velocities (including 10, 25, and 50
297 $\mu\text{m/s}$) are shown in Figure 1c, g, and h (Figure S8 shows the longitudinal section of those
298 hydrogels). Faster ice-growth velocities induced the formation of smaller pores as

299 reported earlier for other polysaccharides [43]. At 50 $\mu\text{m/s}$, the ice front velocity yielded
300 pore surface areas of approximately $2.5 \times 10^3 \mu\text{m}^2$ (Figure 1h), 16% of the value found for
301 10 $\mu\text{m/s}$ ($\approx 1.6 \times 10^4 \mu\text{m}^2$, Figure 1g). This effect is due to the creation of more ice
302 nucleation sites on the bottom of the samples as the ice growth velocity increased, leading
303 to smaller macropores [44]. Overall, we found out that the pore size and their respective
304 distributions can be tuned by modulating the alginate/oxidized cellulose relative
305 composition (Figure 1i and Figure S6a), but also by the ice-growth velocities (Figure 1j
306 and Figure S6b). These values (especially those of A:C=6:2 at 25 $\mu\text{m/s}$ and A:C=4:4 at
307 50 $\mu\text{m/s}$) are comparable to those measured for the xylem of native celery stems
308 ($\approx 1.9 \times 10^3 \mu\text{m}^2$) (Figure S9a and b). In other words, hydrogels reported here, prepared by
309 ice-templating followed by ion-crosslinking, mimic the unidirectional orientation found
310 in plant stems as well as their characteristic dimensions. It is important to note that the
311 biomimetic features of these materials concern not only their structural features, but also
312 their composition, a mixture of polysaccharides close to those found in native plant tissues
313 [45–47].
314



315

316 **Figure 1.** Pictures and SEM images of Ca^{2+} -crosslinked macroporous hydrogels prepared
 317 at $25 \mu\text{m/s}$ (ice growth velocity) using different ratios of alginate and oxidized cellulose:
 318 (a) A:C=8:0, (b) A:C=7:1, (c) A:C=6:2, (d) A:C=4:4, (e) A:C=2:6 and (f) A:C=1:7.
 319 Pictures and SEM images of Ca^{2+} -crosslinked hydrogels prepared at 4:4 ratio of alginate
 320 and oxidized cellulose at different ice front velocities: (g) $10 \mu\text{m/s}$, (h) $50 \mu\text{m/s}$. (i)
 321 Summary of the pore area distribution of alginate and oxidized cellulose macroporous
 322 hydrogels at different compositions for $25 \mu\text{m/s}$ (ice growth velocity) and (j) at different

323 ice front velocities. Moustaches delimit the 5 and 95 percentiles of the distribution and
324 box limits represent the 1st and 3rd quartiles. The rectangles and horizontal lines in the
325 boxes represent mean and median values, respectively. Gray horizontal bars depict the
326 pore area distribution of *A. graveolens* xylem vascular system.

327

328 **3.2. Characterization of topotactic crosslinked hydrogels**

329 *Water stability.* The water stability of hydrogels is one of the most significant features for
330 a variety of applications, including biomedical scaffolds, oil extraction/separation, and
331 water purification/desalination [48,49]. To evaluate the contribution of the proportions of
332 alginate and oxidized cellulose on the water stability, topotactic crosslinked hydrogels
333 with 7 different compositions (prepared with an ice-front velocity of 25 $\mu\text{m/s}$) were
334 immersed in distilled water (Figure S10a) and kept for 30 days at room temperature in
335 static conditions (Figure S10b). At day 30, hydrogels A:C=0:8 were partially dispersed
336 and swollen. On the contrary, all hydrogels containing alginate showed good water
337 stability, suggesting higher alginate contents allow for a more stable crosslinking by
338 calcium ions. These results correlate positively with the higher theoretical crosslinking
339 density for sodium alginate (according to the supplier the carboxyl groups density equals
340 to 5.05 mmol g^{-1} with a M/G ratio of 1.56, which amounts to *c.a.* 2.0 mmol g^{-1} of G units)
341 in comparison with that of oxidized cellulose (carboxyl groups density equal to 0.76
342 mmol g^{-1}). In general, polysaccharide materials prepared by ice templating redisperse
343 readily in water unless cryogelation occurs [50] or postprocessing steps are added, such
344 as photo-crosslinking or photo-polymerization. [51–56]. Here, we demonstrate that self-
345 supported hydrogels with long term water stability can be achieved via ice-templating
346 followed by ion crosslinking during thawing, without further stabilization by photo-
347 polymerization or photo-crosslinking. Moreover, the components used for the photo-

348 induced gelation rely on particularly harmful components for the environment and are
349 especially difficult to implement in complex, 3D geometries. Ice templating coupled to
350 topotactic stabilization eliminates these bottlenecks in a straightforward and non-toxic
351 process.

352

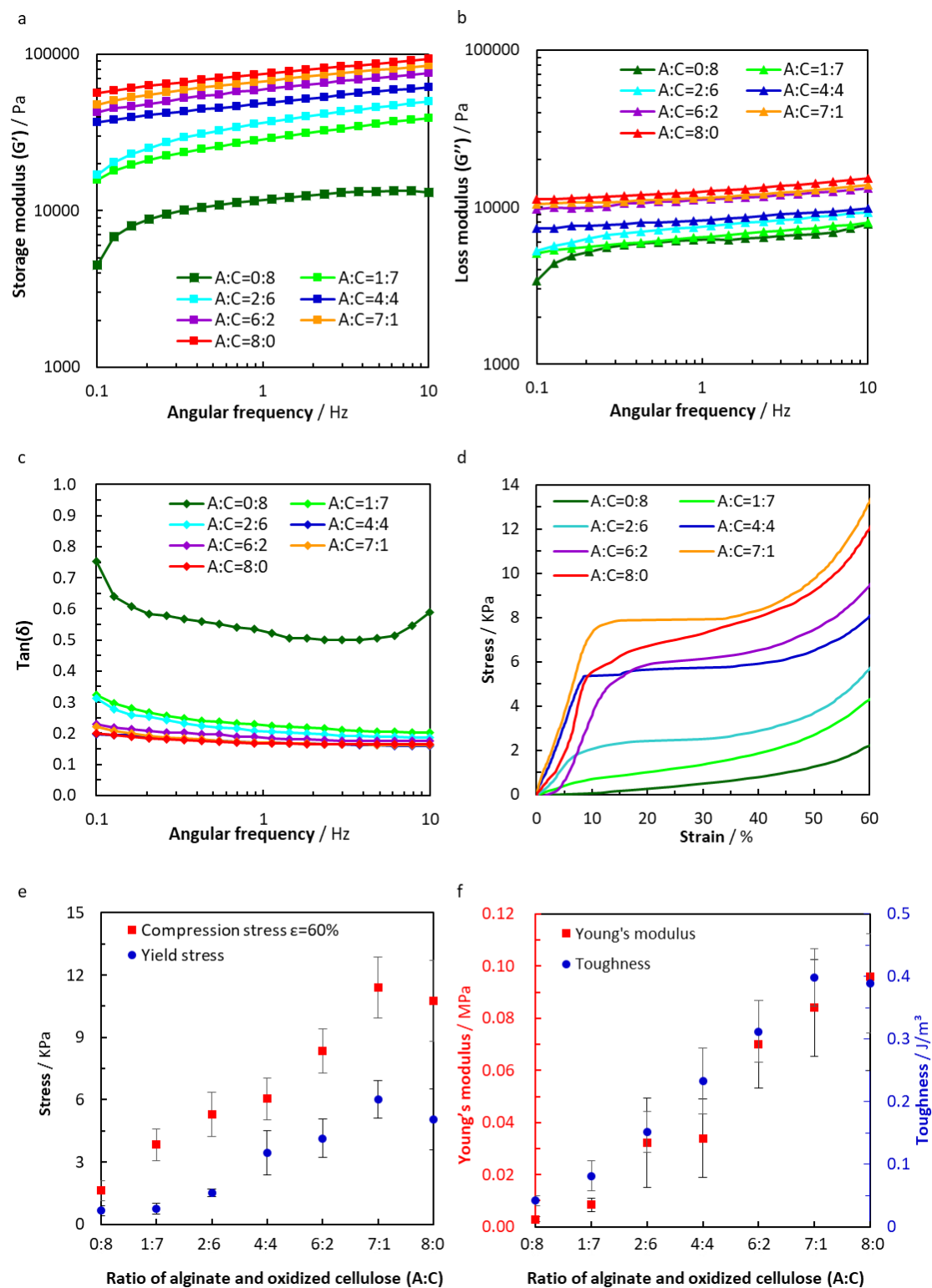
353 *Viscoelastic properties.* The viscoelastic properties of hydrogels determine, to a large
354 extent, their applicability for a wide range of uses. To ascertain the viscoelastic properties
355 of the macroporous hydrogels, frequency sweep measurements were carried out on
356 crosslinked suspensions obtained through Ca^{2+} -crosslinking at different alginate/oxidized
357 cellulose components. The storage modulus (G'), loss modulus (G''), and damping factor
358 ($\tan(\delta) = G''/G'$) as functions of frequency are shown in Figure 2a, b, and c. All the
359 compositions of alginate/oxidized cellulose showed a gel-like behavior ($G' > G''$) over
360 the entire angular frequency range, indicating that both alginate and oxidized cellulose
361 formed a crosslinked structure with Ca^{2+} . The decrease of $\tan(\delta)$ with alginate content
362 suggests that in presence of Ca^{2+} ions, this polysaccharide promotes a more solid-like and
363 stiffer internal network to the hydrogels, as previously seen for the water swelling
364 experiments. These observations are equally confirmed by the absolute values of G' and
365 G'' . Both values increase with the fraction of alginate, and in both, the values are mostly
366 independent from the angular frequency.

367 The ratio between the two polysaccharides provides a tool to tailor the characteristic pore
368 size and to modulate the crosslinking density inside the hydrogel and, as a consequence,
369 a lever to tune their viscoelastic properties.

370

371 *Mechanical properties.* To investigate the effects of the composition of alginate and

372 cellulose on the hydrogels, compression tests were performed uniaxially along the
373 freezing direction on macroporous hydrogels prepared from different ratios of
374 alginate/oxidized cellulose with a constant ice growth velocity of 25 $\mu\text{m/s}$. The resulting
375 stress-strain curves are shown in Figure 2d, and their mechanical properties are described
376 in Table S1. All stress-strain curves present an equivalent behavior, with an initial slope
377 corresponding to an elastic deformation regime, followed by a yield point and a plateau,
378 which evolves to reach a densification regime. The compression stress at 60% strain and
379 the yield stress are summarized in Figure 2e, and the Young's modulus and toughness of
380 the hydrogels are summed up in Figure 2f. All measured properties increased with
381 increasing ratio of alginate, with exception for the A:C = 8:0 sample. The A:C=7:1 sample
382 resulted in the highest compression stress, yield stress, and toughness. This optimum
383 value is ascribed to the reinforcement of the alginate hydrogel matrix by low volume
384 fractions of oxidized cellulose, which is likely to favor even dispersion of the filler. At
385 higher volume fractions oxidized cellulose is expected to aggregate and entangle,
386 providing a less effective reinforcement effect. At A:C=7:1 ratio, hydrogels featured an
387 improvement in compression and yield stress up to 107% and 119%, respectively, in
388 comparison to A:C=8:0. Taking into account that this material (A:C=7:1) has the smallest
389 pore area distribution (Figure S6a), it is impossible to ascribe the enhancement of the
390 mechanical properties exclusively to the composite nature of the hydrogels or the
391 rheology of the suspensions, and the size and morphology of the pores should equally be
392 considered.



393

394 **Figure 2.** Viscoelastic properties of crosslinked gels with different compositions of
 395 alginate and oxidized cellulose (prepared with an ice growth velocity of $25 \mu\text{m/s}$) (a)
 396 storage modulus, (b) loss modulus, and (c) damping factor. Compression test results of

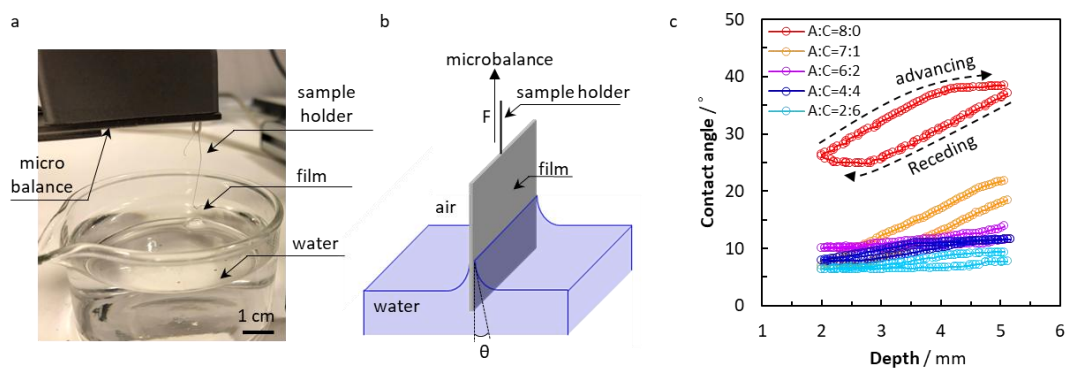
397 crosslinked hydrogels prepared from different ratios of alginate and oxidized cellulose at
398 an ice growth velocity of 25 $\mu\text{m/s}$ (d) Compression strain-stress curves, (e) compression
399 stress at 60% of strain and yield stress, (f) Young's modulus and toughness.

400

401 3.3. Dynamic contact angle measurement

402 To assess the wettability dynamics of various hydrogel compositions, we measured the
403 contact angles at the triphase line formed by the films deposited on glass slides, water,
404 and air during dipping and retraction stages (Figure 3a-c). At 38°, A:C=8:0 featured the
405 highest advancing contact angle and it scaled monotonically with the oxidized cellulose
406 contents, reaching 9° for A:C=2:6. This trend is in good agreement with the observations
407 of Montrezor *et al.*, who measured the contact angle for non-crosslinked alginate and
408 oxidized cellulose samples [57]. Although the geometric aspects of these films may differ
409 from the walls inside the hydrogels prepared by ice-templating, their surface chemistry
410 should be strictly comparable. In this sense, the values measured here provide valuable
411 information to describe the wettability of hydrogels of different polysaccharide
412 composition.

413



414

415 **Figure 3.** (a) Photo and (b) schematic illustration of the dynamic contact angle
416 measurements made with a tensiometer. (c) Hysteresis of the dynamic contact angle
417 measurement for films prepared from different ratios of alginate/oxidized cellulose.

418

419 **3.4. Liquid transport measurement**

420 The previous sections have shown that it is possible to control pore size inside the
421 macroporous polysaccharide hydrogels by tuning the ice-growth velocities or the
422 alginate/oxidized cellulose ratio. Furthermore, the wettability measurements demonstrate
423 the influence of composition on the water contact angle. Given the significant roles of
424 pore size and wettability in water transport within biological structures, we have
425 conducted measurements of this property in macroporous polysaccharide hydrogels
426 fabricated through ice templating and topotactic crosslinking. Water transport within
427 cross-linked hydrogels obtained at different ice-growth velocities (10, 25, and 50 $\mu\text{m/s}$)
428 and different ratios of alginate/oxidized cellulose was measured and compared to the
429 water transport properties found for decellularized stem of celery. To ensure that the
430 experimental setup accurately measured the transport of liquid within the pores, rather
431 than the diffusion of dye through the pore walls, a control experiment was conducted.
432 This involved exposing single polysaccharide walls to the dye (methylene blue, MB)
433 under the same conditions (Figure S11). As no measurable diffusion of the dye in the pore
434 walls was detected within the relevant time frame (60 minutes), we confirmed that all
435 observations of dye progression in the hydrogels corresponded to liquid transport inside
436 the pores.

437 Compositions A:C=6:2, 4:4, and 2:6 were chosen as they reproduce more accurately the
438 global fraction of cellulose in plant stems (approximately 30-80% cellulose) [58,59]. The
439 experimental setup for liquid transport is depicted in Figure 4a and b, and images of liquid
440 transport behaviors inside hydrogels—prepared at different ice-growth velocities—up to
441 60 minutes are shown in Figure 4c and d, respectively. Plotting the curves of rising height
442 of liquid versus time (Figure 4e and f for different ice-growth velocities and ratios,

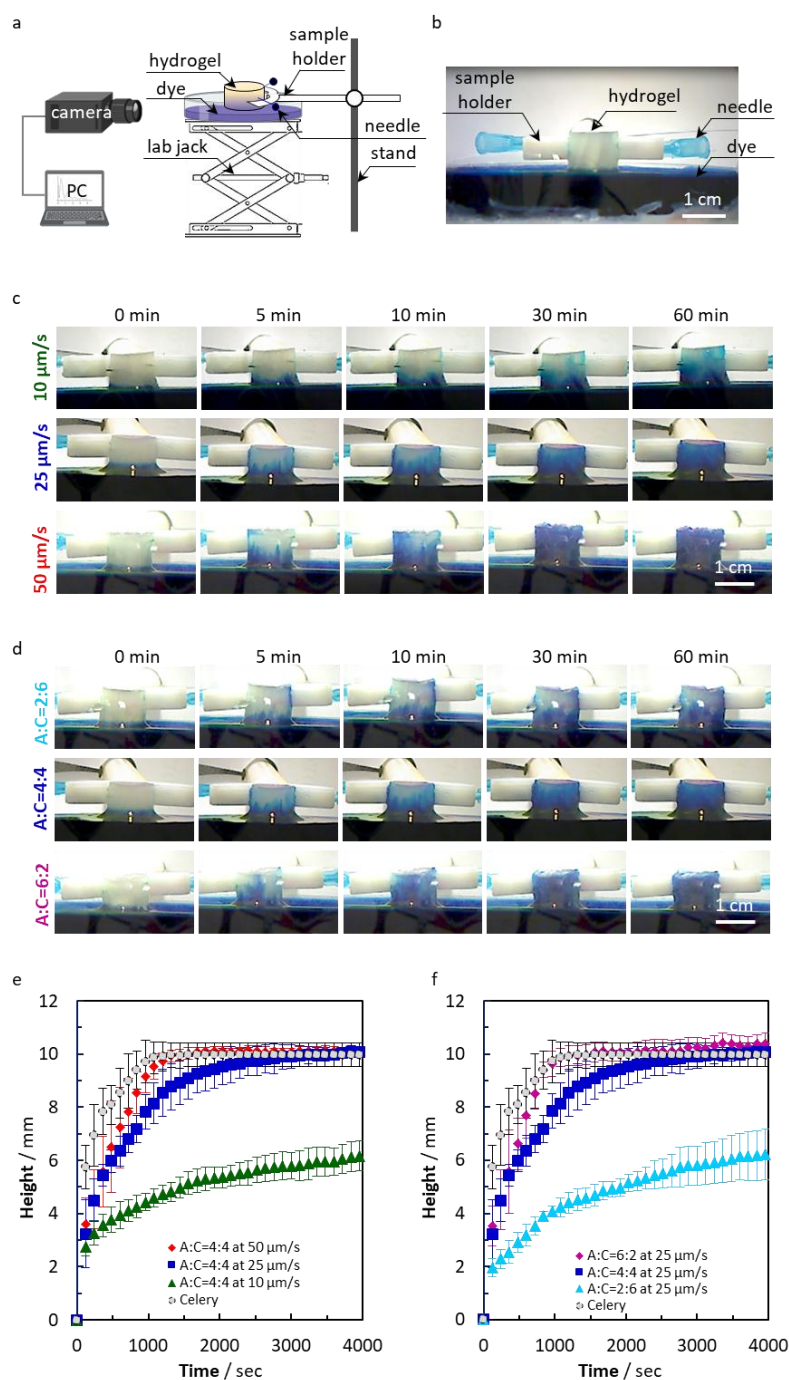
443 respectively) shows that the ascending speed through anisotropic hydrogels is faster in
444 the initial stages followed by a slower regime. For a given composition, the rising speed
445 of liquid within the hydrogels prepared at 50 $\mu\text{m/s}$ was the highest and it decreased
446 consistently for samples prepared at slower ice-growth velocities. This observation
447 underscores the significant influence of ice front velocity, and consequently pore size
448 variation, on regulating the liquid transport velocities of the resultant hydrogels, despite
449 their identical compositions.

450 For hydrogels with different ratios of alginate/oxidized cellulose, the elapsed time before
451 the liquid reached the top of the sample (height = 10 mm) varied with the composition.
452 For sample A:C=6:2 the elapsed time was around 1440 s whereas for sample A:C=4:4
453 the required time was as high as 3240 s. In addition, in contact with sample A:C=2:6, the
454 liquid did not reach the top of the hydrogel within 60 mins. Although these findings align
455 with the hydrogels' composition and, consequently, the samples' wettability. It is
456 important to highlight that the characteristic contact angles fall within a narrow range,
457 spanning from 9 to 14°. This limited variation hardly accounts for the significant
458 differences observed in transport properties. On the contrary, the pore distribution in the
459 same samples ranges from approximately $3\text{-}16 \times 10^3 \mu\text{m}^2$, suggesting this parameter plays
460 a predominant role in liquid transport properties. Lower contact angle should translate to
461 a higher capillary coefficient—and thus faster capillary water transport according to
462 Lucas-Washburn equation [60,61]. However, our observations contradict this trend,
463 reinforcing the predominant role of the pores' dimensions and the arrangement of pores
464 in relation to each other in controlling the capillary transport within the macroporous
465 hydrogels reported here.

466 Celery was used as a native plant tissue reference for comparing the capillary rising

467 behavior of the prepared hydrogels. The decellularized and bleached celery allowed for
468 the visualization of dye rising from the bottom to the top of the celery stem sample (Figure
469 S12a). In living vascular plants, leaves facilitate transpiration. The resulting evaporation
470 generates a vapor pressure depression which promotes capillary liquid transport through
471 the plant stem. However, in this study, liquid was transported up the celery stem without
472 leaves, reaching the top after around 1000 seconds (Figure 4e and f, and Figure S12b).
473 Although the celery's initial rising speed was much faster than the prepared hydrogels, it
474 became comparable to hydrogels, especially for A:C=6:2 at 25 $\mu\text{m/s}$ and A:C=4:4 at 50
475 $\mu\text{m/s}$. In other words, the hydrogels prepared with alginate and oxidized cellulose via ice-
476 templating in this study successfully mimic both the structural features of plant stems and
477 their liquid transport behavior.

478 In summary, we successfully created bioinspired hydrogels through ice-templating/ion-
479 crosslinking of alginate and oxidized cellulose suspensions. By adjusting precursor
480 compositions and ice growth velocities, we could control mechanical, surface properties,
481 and morphologies. The resulting hydrogels exhibit capillary water transport behavior
482 primarily dependent on pore size and the alignment of pores in relation to each other.
483 These tunable features make the hydrogels highly suitable for biomedical applications,
484 such as drug delivery systems and wound dressings, where controlled moisture retention,
485 capillary action, and the gradual release of therapeutic agents are essential. Additionally,
486 from an environmental standpoint, these hydrogels have potential applications in water
487 filtration systems, where their capillary action and adjustable porosity facilitate the
488 efficient removal of contaminants.



489
 490 **Figure 4.** Liquid transport experiment with different composition of alginate and oxidized
 491 cellulose and with different ice-growth velocity. (a) Schematic illustration of the liquid
 492 transport experimental setup, (b) the photo through the lens of the camera during liquid
 493 transport experiment. Optical photos showing capillary action behavior with the hydrogel
 494 prepared at (c) different ice growth velocities (A:C = 4:4) and (d) with different
 495 compositions of alginate and oxidized cellulose (ice growth velocity 25 μm/s). (e) Time-
 496 liquid height curves with A:C = 4:4 at different ice-growth velocity. (f) Time-liquid height

497 curves with hydrogels obtained by different compositions of alginate and oxidized
498 cellulose with ice growth velocity of 25 $\mu\text{m/s}$.

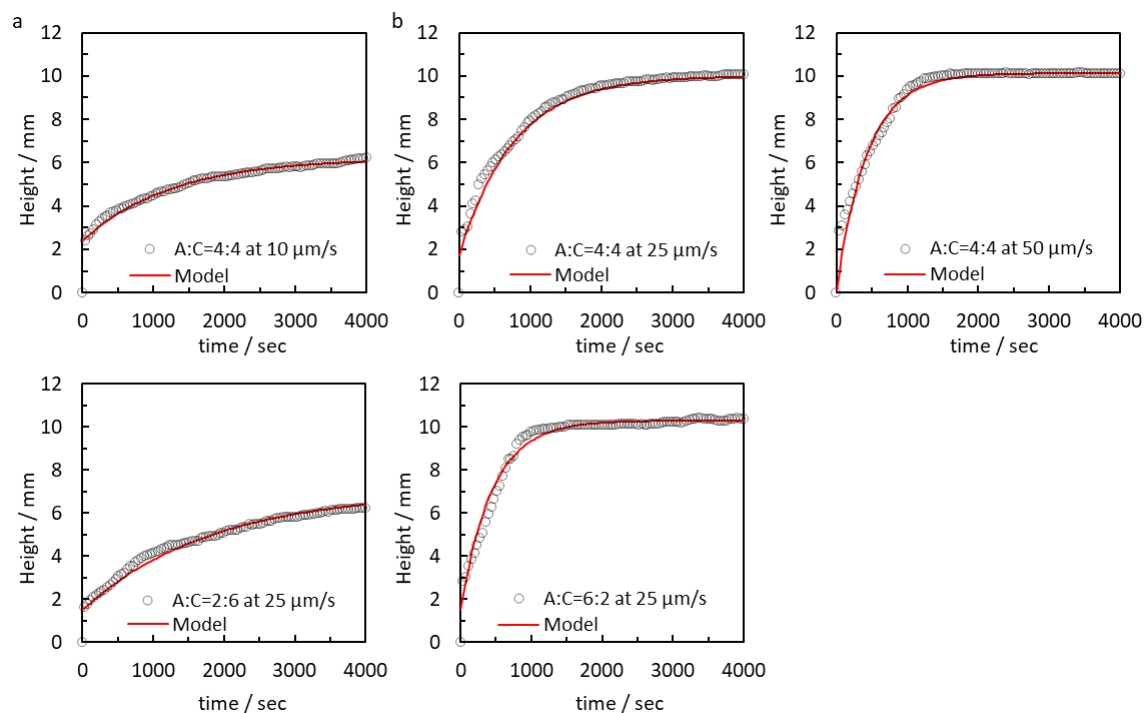
499

500 In general, porous media can be characterized by studying the kinetics of liquid rise within
501 the pore spaces. Although porous media generally have a complex structure, they can be
502 modeled as a single, vertical capillary or as an assembly of such capillaries. The main
503 difficulties lie in separately estimating the effective mean radius of the capillaries and the
504 contact angle between the liquid and the pore. In the characterization of porous media by
505 capillary rise, the dynamic properties of the liquid front and any meniscus deformation or
506 dynamic contact angle effects will have important consequences. Specifically, we
507 consider that the contact angle between the liquid meniscus and the inner surface of the
508 capillary becomes a dynamic contact angle when the liquid front is in movement as shown
509 in the hysteresis study of the contact angle (Figure 3c). It has previously been
510 demonstrated that the resulting time dependence is due to frictional dissipation at the
511 moving wetting front. In modeling the conducted experiments, we employ an analytical
512 expression for height versus time, facilitating the determination of the retardation
513 coefficient. This coefficient encompasses both diffusion and friction contributions to
514 dissipation [62]. Here, we utilize the analytical equation established by Hamraoui *et al.*
515 [63].

$$516 \quad h(t) = h_e + (h(0) - h_e) \exp \left[-\frac{\gamma \cos(\theta_0)}{\beta_1 h_e} t \right] \quad (\text{eq. 1})$$

517 where β_1 is the slowdown coefficient, θ_0 is the equilibrium contact angle, γ surface
518 tension of the used liquid, $h(t = 0)$ and $h_e = h(t \rightarrow \infty)$ are respectively the initial
519 and the equilibrium heights. In this scenario, the fitting process required only β_1 as a
520 parameter, with the pore radius implicitly incorporated into h_e , which is determined

521 experimentally. The experimental curve fits, presented in Figure 5, were carried out using
 522 the analytical expression given in equation (E1). Across all experimental curves,
 523 including sample prepared with different composition (A:C=2:6-6:2) of polysaccharide
 524 and with different ice-growth velocities (at 10-50 $\mu\text{m/s}$), a consistent match with fitting
 525 model curves is observed. Table 2 gathers the retardation coefficients calculated for each
 526 sample. The retardation coefficients in sample A:C=2:6 at 25 $\mu\text{m/s}$ and A:C=4:4 at 10
 527 $\mu\text{m/s}$ are relatively lower ($\beta_1 \approx 13$ and 17 for A:C=2:6 at 25 $\mu\text{m/s}$ and A:C=4:4 at 10
 528 $\mu\text{m/s}$, respectively), while those for A:C=6:2 at 25 $\mu\text{m/s}$ and A:C=4:4 at 50 $\mu\text{m/s}$ exhibited
 529 higher values ($\beta_1 \approx 2.8$). This observation aligns well with the experimental data of the
 530 liquid height profile, emphasizing the pivotal role of pore size in the liquid transport
 531 behavior within the macroporous hydrogels.



532
 533 **Figure 5.** The graphs illustrate the capillary water transport behavior within hydrogels,
 534 which were prepared with varying ice-growth velocities (a-c) and distinct compositions
 535 of alginate and oxidized cellulose (d and e), along with the theoretical fitting curves as
 536 defined by eq. 1.

537

538 In the liquid transport behavior within the macroporous hydrogels, diffusion plays a
539 crucial role in governing the initial stages of the liquid transport. This stage is guided by
540 the pressure gradients generated by the impulsive force, such as the wetting stress. Figure
541 S13a-e displays fitting curves on the experimental $h(t)$ profiles at short times by using
542 diffusion equation $h(t)^2 = 6Dt$, where D denotes diffusion coefficient, and t denotes
543 time. The revealed values of diffusion coefficient highlight a trend where the hydrogels
544 with smaller pore size, such as A:C=4:4 at 10 $\mu\text{m/s}$ and A:C=6:2 at 25 $\mu\text{m/s}$, yielded
545 higher diffusion coefficients. Figure S13f illustrates the findings, indicating an inverse
546 correlation between the diffusion coefficient and the retardant coefficients. Notably,
547 hydrogels with smaller pore sizes displayed lower retardation coefficients. These
548 variations in the diffusion coefficients among samples indicate that the contribution of
549 the friction at the triple phase line—defined by polysaccharide walls, air, and water—is
550 relatively equivalent for sample A:C=4:4 at 10 $\mu\text{m/s}$ and A:C=2:6 at 25 $\mu\text{m/s}$ but
551 considerably lower than that along a three-phase line of sample A:C=6:2 at 25 $\mu\text{m/s}$ and
552 A:C=4:4 at 50 $\mu\text{m/s}$.

553 In summary, this study demonstrates the impact of the intricate correlation between pore
554 size, diffusion coefficients, and retardation coefficients on liquid transport within
555 macroporous hydrogels. It also highlights the central roles of diffusion as the driving force
556 for liquid movement within the pores and friction at the triphase line responsible for the
557 dynamic nature of the contact angle.

558

559 **Table 2.** Retardation coefficients and diffusion coefficients (D) of samples prepared
560 with different ice-growth velocities/compositions of alginate and oxidized cellulose.

Sample	Retardation coefficient	D (mm ² s ⁻²)
A:C=4:4 at 10 μm/s	12.85	0.00072
A:C=4:4 at 25 μm/s	4.91	0.00600
A:C=4:4 at 50 μm/s	2.76	0.01457
A:C=2:6 at 25 μm/s	16.60	0.00103
A:C=6:2 at 25 μm/s	2.78	0.01630

561

562 **4. Conclusions**

563 Anisotropic macroporous hydrogels, inspired by the structural features of plant stems,
564 were successfully fabricated using alginate and oxidized cellulose through ice-templating
565 followed by topotactic ion-crosslinking with Ca²⁺, a strategy previously developed in our
566 team to stabilize protein-based biomaterials. The resulting ionic crosslinking rendered the
567 hydrogels insoluble in water. By adjusting the overall amounts of alginate and oxidized
568 cellulose, tunable viscoelastic properties and wettability were achieved, aligning with the
569 respective compositions of alginate and oxidized cellulose. Remarkably, introducing a
570 minimal quantity of oxidized cellulose in the crosslinked hydrogels effectively reinforced
571 the alginate matrix, leading to the highest mechanical properties. Moreover, the
572 morphological characteristics of the hydrogels were tunable, influenced not only by the
573 ice growth speed but also by the composition. These levers allowed to obtain pore sizes
574 comparable with those found in the xylem of celery and, more importantly, to reproduce
575 the plant stems' liquid transport behavior. In fact, capillary liquid transport experiments
576 demonstrated that crosslinked anisotropic hydrogels with smaller pore sizes exhibited
577 faster liquid rising speeds, comparable to those observed in celery. These findings

578 highlight the potential applications of these hydrogels as biomimetic scaffolds in
579 biomedical fields or water purification systems, capitalizing on their anisotropic
580 architecture and their biocompatible composition.

581

582 **5. Acknowledgement**

583 This work was supported by both the Paris Ile-de France Region - DIM Respire, and The
584 French Embassy in Tokyo through Bourses France Excellence and by French state funds
585 managed by the National Research Agency (ANR) through the CellsInFoams project,
586 grant n. ANR-17-CE08-0009 and Emerge project (grant n. ANR-19-CE08-0023)

587

588 **6. Conflicts of Interest**

589 The authors declare that they have no known competing financial interests or personal
590 relationships that could have appeared to influence the work reported in this paper.

591

592 **7. Data availability**

593 The data supporting this article have been included as part of the Supplementary
594 Information.

595

596 **8. CRediT author statement**

597 Katsuya KOMIYAMA: Investigation, Writing - Original Draft. Maya ALLARD:
598 Investigation. Corentin ESCHENBRENNER: Investigation. Ahmed HAMRAOUI:
599 Investigation. Clémence SICARD: Writing - Review & Editing, Supervision, Funding
600 acquisition. Francisco M. FERNANDES: Conceptualization, Writing - Review & Editing,

601 Supervision, Funding acquisition

602

603 **9. References**

- 604 [1] T.I. Baskin, Anisotropic expansion of the plant cell wall, *Annu Rev Cell Dev Biol*
605 **21** (2005) 203–222.
- 606 [2] W. Kong, C. Wang, C. Jia, Y. Kuang, G. Pastel, C. Chen, G. Chen, S. He, H. Huang,
607 J. Zhang, S. Wang, L. Hu, Muscle-Inspired Highly Anisotropic, Strong, Ion-
608 Conductive Hydrogels, *Adv Mater* **30** (2018) 1–7.
- 609 [3] P. Calvert, Hydrogels for soft machines, *Adv Mater* **21** (2009) 743–756.
- 610 [4] M.J. Hancock, K. Sekeroglu, M.C. Demirel, Bioinspired directional surfaces for
611 adhesion, wetting, and transport, *Adv Funct Mater* **22** (2012) 2223–2234.
- 612 [5] J. Radhakrishnan, A. Subramanian, U.M. Krishnan, S. Sethuraman, Injectable and
613 3D Bioprinted Polysaccharide Hydrogels: From Cartilage to Osteochondral Tissue
614 Engineering, *Biomacromolecules* **18** (2017) 1–26.
- 615 [6] P. Datta, V. Vyas, S. Dhara, A.R. Chowdhury, A. Barui, Anisotropy Properties of
616 Tissues: A Basis for Fabrication of Biomimetic Anisotropic Scaffolds for Tissue
617 Engineering, *J Bionic Eng* **16** (2019) 842–868.
- 618 [7] M.H. Cai, X.Y. Chen, L.Q. Fu, W.L. Du, X. Yang, X.Z. Mou, P.Y. Hu, Design
619 and Development of Hybrid Hydrogels for Biomedical Applications: Recent
620 Trends in Anticancer Drug Delivery and Tissue Engineering, *Front Bioeng*
621 *Biotechnol* **9** (2021) 1–18.
- 622 [8] S. Murdan, Electro-responsive drug delivery from hydrogels, *J Control Release* **92**
623 (2003) 1–17.
- 624 [9] N. Annabi, K. Tsang, S.M. Mithieux, M. Nikkhah, A. Ameri, A. Khademhosseini,
625 A.S. Weiss, Highly elastic micropatterned hydrogel for engineering functional
626 cardiac tissue, *Adv Funct Mater* **23** (2013) 4950–4959.
- 627 [10] M. Nikkhah, N. Eshak, P. Zorlutuna, N. Annabi, M. Castello, K. Kim, A.
628 Dolatshahi-Pirouz, F. Edalat, H. Bae, Y. Yang, A. Khademhosseini, Directed
629 endothelial cell morphogenesis in micropatterned gelatin methacrylate hydrogels,
630 *Biomater* **33** (2012) 9009–9018.
- 631 [11] Z. Chen, D. Zhao, B. Liu, G. Nian, X. Li, J. Yin, S. Qu, W. Yang, 3D Printing of
632 Multifunctional Hydrogels, *Adv Funct Mater* **29** (2019) 1–8.
- 633 [12] T. Distler, A.R. Boccaccini, 3D printing of electrically conductive hydrogels for
634 tissue engineering and biosensors – A review, *Acta Biomater* **101** (2020) 1–13.

- 635 [13] M.A. Haque, G. Kamita, T. Kurokawa, K. Tsujii, J.P. Gong, Unidirectional
636 alignment of lamellar bilayer in hydrogel: One-dimensional swelling, anisotropic
637 modulus, and stress/strain tunable structural color, *Adv Mater* **22** (2010) 5110–
638 5114.
- 639 [14] X.Y. Lin, Z.J. Wang, P. Pan, Z.L. Wu, Q. Zheng, Monodomain hydrogels prepared
640 by shear-induced orientation and subsequent gelation, *RSC Adv* **6** (2016) 95239–
641 95245.
- 642 [15] J.M. Jang, S.H.T. Tran, S.C. Na, N.L. Jeon, Engineering controllable architecture
643 in Matrigel for 3D cell alignment, *ACS Appl Mater Interfaces* **7** (2015) 2183–2188.
- 644 [16] Q. Lu, S. Bai, Z. Ding, H. Guo, Z. Shao, H. Zhu, D.L. Kaplan, Hydrogel Assembly
645 with Hierarchical Alignment by Balancing Electrostatic Forces, *Adv Mater*
646 *Interfaces* **3** (2016) 1–6.
- 647 [17] W. Shi, J. Huang, R. Fang, M. Liu, Imparting Functionality to the Hydrogel by
648 Magnetic-Field-Induced Nano-assembly and Macro-response, *ACS Appl Mater*
649 *Interfaces* **12** (2020) 5177–5194.
- 650 [18] K. Qin, C. Parisi, F.M. Fernandes, Recent advances in ice templating: From
651 biomimetic composites to cell culture scaffolds and tissue engineering, *J Mater*
652 *Chem B* **9** (2021) 889–907.
- 653 [19] E. Thibert, F. Dominé, Thermodynamics and Kinetics of the Solid Solution of HCl
654 in Ice, *J Phys Chem B* **101** (1997) 3554–3565.
- 655 [20] E. Thibert, F. Dominé, Thermodynamics and Kinetics of the Solid Solution of
656 HNO₃ in Ice, *J Phys Chem B* **102** (1998) 4432–4439.
- 657 [21] T. Köhnke, T. Elder, H. Theliander, A.J. Ragauskas, Ice templated and cross-
658 linked xylan/nanocrystalline cellulose hydrogels, *Carbohydr Polym* **100** (2014)
659 24–30.
- 660 [22] K. Yan, F. Xu, S. Li, Y. Li, Y. Chen, D. Wang, Ice-templating of chitosan/agarose
661 porous composite hydrogel with adjustable water-sensitive shape memory
662 property and multi-staged degradation performance, *Colloids Surf B Biointerfaces*
663 **190** (2020) 110907.
- 664 [23] S. Christoph, J. Kwiatoszynski, T. Coradin, F.M. Fernandes, Cellularized Cellular
665 Solids via Freeze-Casting, *Macromol Biosci* **16** (2016) 182–187.
- 666 [24] P. Sikorski, F. Mo, G. Skjåk-Bræk, B.T. Stokke, Evidence for egg-box-compatible
667 interactions in calcium - Alginate gels from fiber x-ray diffraction,
668 *Biomacromolecules* **8** (2007) 2098–2103.
- 669 [25] A. Isogai, T. Saito, H. Fukuzumi, TEMPO-oxidized cellulose nanofibers,
670 *Nanoscale* **3** (2011) 71–85.

- 671 [26] H. Dong, J.F. Snyder, K.S. Williams, J.W. Andzelm, Cation-induced hydrogels of
672 cellulose nanofibrils with tunable moduli, *Biomacromolecules* **14** (2013) 3338–
673 3345.
- 674 [27] N. Masruchin, B.D. Park, V. Causin, I.C. Um, Characteristics of TEMPO-oxidized
675 cellulose fibril-based hydrogels induced by cationic ions and their properties,
676 *Cellulose* **22** (2015) 1993–2010.
- 677 [28] T. Guo, Y. Pei, K. Tang, X. He, J. Huang, F. Wang, Mechanical and drug release
678 properties of alginate beads reinforced with cellulose, *J Appl Polym Sci* **134** (2017)
679 44495.
- 680 [29] L.F. Wang, S. Shankar, J.W. Rhim, Properties of alginate-based films reinforced
681 with cellulose fibers and cellulose nanowhiskers isolated from mulberry pulp,
682 *Food Hydrocoll* **63** (2017) 201–208.
- 683 [30] T. Huq, S. Salmieri, A. Khan, R.A. Khan, C. Le Tien, B. Riedl, C. Fraschini, J.
684 Bouchard, J. Uribe-Calderon, M.R. Kamal, M. Lacroix, Nanocrystalline cellulose
685 (NCC) reinforced alginate based biodegradable nanocomposite film, *Carbohydr*
686 *Polym* **90** (2012) 1757–1763.
- 687 [31] C. Rieu, C. Parisi, G. Mosser, B. Haye, T. Coradin, F.M. Fernandes, L. Trichet,
688 Topotactic Fibrillogenesis of Freeze-Cast Microridged Collagen Scaffolds for 3D
689 Cell Culture, *ACS Appl Mater Interfaces* **11** (2019) 14672–14683.
- 690 [32] T. Saito, A. Isogai, TEMPO-Mediated Oxidation of Native Cellulose. The Effect
691 of Oxidation Conditions on Chemical and Crystal Structures of the Water-
692 Insoluble Fractions, *Biomacromolecules* **5** (2004) 1983–1989.
- 693 [33] J. Esmaili, S. Jadbabae, F.M. Far, M.E. Lukolayeh, K.K. Kirboğa, F.S. Rezaei,
694 A. Barati, Decellularized *Alstroemeria* flower stem modified with chitosan for
695 tissue engineering purposes: A cellulose/chitosan scaffold, *Int J Biol Macromol*
696 **204** (2022) 321–332.
- 697 [34] C. Stolze, T. Janoschka, U.S. Schubert, F.A. Müller, S. Flauder, Directional
698 Solidification with Constant Ice Front Velocity in the Ice-Templating Process, *Adv*
699 *Eng Mater* **18** (2016) 111–120.
- 700 [35] D. Legland, I. Arganda-Carreras, P. Andrey, MorphoLibJ: Integrated library and
701 plugins for mathematical morphology with ImageJ, *Bioinformatics* **32** (2016)
702 3532–3534.
- 703 [36] J. Schindelin, I. Arganda-Carreras, E. Frise, V. Kaynig, M. Longair, T. Pietzsch,
704 S. Preibisch, C. Rueden, S. Saalfeld, B. Schmid, J.Y. Tinevez, D.J. White, V.
705 Hartenstein, K. Eliceiri, P. Tomancak, A. Cardona, Fiji: An open-source platform
706 for biological-image analysis, *Nat Methods* **9** (2012) 676–682.

- 707 [37] O.N. Tretinnikov, Y. Ikada, Dynamic Wetting and Contact Angle Hysteresis of
708 Polymer Surfaces Studied with the Modified Wilhelmy Balance Method,
709 *Langmuir* **10** (1994) 1606–1614.
- 710 [38] S. Ardizzonea, G. Gabriellib, P. Lazzarib, Adsorption of Methylene Blue at
711 solid/liquid and water/air interfaces, *Colloids Surf A Physicochem Eng Asp* **16**
712 (1993) 149–57.
- 713 [39] C. Rodríguez-Rivero, L. Hilliou, E.M. Martín del Valle, M.A. Galán, Rheological
714 characterization of commercial highly viscous alginate solutions in shear and
715 extensional flows, *Rheol Acta* **53** (2014) 559–570.
- 716 [40] E.A. Pinto, J.L. Dávila, M.A. d’Ávila, Rheological studies on nanocrystalline
717 cellulose/alginate suspensions, *J Mol Liq* **277** (2019) 418–423.
- 718 [41] I. Nelson, S.E. Naleway, Intrinsic and extrinsic control of freeze casting, *J Mater*
719 *Res Technol* **8** (2019) 2372–2385.
- 720 [42] B. Thomas, S. Geng, J. Wei, H. Lycksam, M. Sain, K. Oksman, Ice-Templating of
721 Lignin and Cellulose Nanofiber-Based Carbon Aerogels: Implications for Energy
722 Storage Applications, *ACS Appl Nano Mater* **5** (2022) 7954–7966.
- 723 [43] S. Christoph, P. Barré, B. Haye, T. Coradin, F.M. Fernandes, Environmentally-
724 stable eco-friendly pectin-silica bio-hybrid foams for soil remediation, *Giant* **12**
725 (2022) 100119.
- 726 [44] S. Deville, Ice-templating, freeze casting: Beyond materials processing, *J Mater*
727 *Res* **28** (2013) 2202–2219.
- 728 [45] K.A. Khalid, A.A. Ahmad, T.L.-K. Yong, Lignin Extraction from Lignocellulosic
729 Biomass Using Sub- and Supercritical Fluid Technology as Precursor for Carbon
730 Fiber Production, *J Jpn Inst Energy* **96** (2017) 255–260.
- 731 [46] P. Ghanney, J.X. Kugbe, D.K. Anning, Role of Microbial Biomechanics in
732 Composting with Special Reference to Lignocellulose Biomass Digestion, *Asian J*
733 *Biotechnol Bioresour Technol* (2021) 30–46.
- 734 [47] J.U. Hernández-Beltrán, I.O. Hernández-De Lira, M.M. Cruz-Santos, A. Saucedo-
735 Luevanos, F. Hernández-Terán, N. Balagurusamy, Insight into Pretreatment
736 Methods of Lignocellulosic Biomass to Increase Biogas Yield: Current State,
737 Challenges, and Opportunities, *Appl Sci* **9** (2019) 3721.
- 738 [48] E.M. Ahmed, Hydrogel: Preparation, characterization, and applications: A review,
739 *J Adv Res* **6** (2015) 105–121.
- 740 [49] X. Zhou, Y. Guo, F. Zhao, G. Yu, Hydrogels as an Emerging Material Platform
741 for Solar Water Purification, *Acc Chem Res* **52** (2019) 3244–3253.
- 742 [50] V.I. Lozinsky, O. Okay, Basic Principles of Cryotropic Gelation, *Adv Polym Sci*

- 743 **263** (2014) 49–101.
- 744 [51] H. Bai, A. Polini, B. Delattre, A.P. Tomsia, Thermoresponsive composite
745 hydrogels with aligned macroporous structure by ice-templated assembly, *Chem*
746 *Mater* **25** (2013) 4551–4556.
- 747 [52] M. Barrow, H. Zhang, Aligned porous stimuli-responsive hydrogels via directional
748 freezing and frozen UV initiated polymerization, *Soft Matter* **9** (2013) 2723–2729.
- 749 [53] J. Wu, Q. Zhao, J. Sun, Q. Zhou, Preparation of poly(ethylene glycol) aligned
750 porous cryogels using a unidirectional freezing technique, *Soft Matter* **8** (2012)
751 3620–3626.
- 752 [54] J. Wu, Y. Lin, J. Sun, Anisotropic volume change of poly(N-isopropylacrylamide)-
753 based hydrogels with an aligned dual-network microstructure, *J Mater Chem* **22**
754 (2012) 17449–17451.
- 755 [55] M. Barrow, A. Eltmimi, A. Ahmed, P. Myers, H. Zhang, Frozen polymerization
756 for aligned porous structures with enhanced mechanical stability, conductivity, and
757 as stationary phase for HPLC, *J Mater Chem* **22** (2012) 11615–11620.
- 758 [56] M. Chen, J. Zhu, G. Qi, C. He, H. Wang, Anisotropic hydrogels fabricated with
759 directional freezing and radiation-induced polymerization and crosslinking method,
760 *Mater Lett* **89** (2012) 104–107.
- 761 [57] L.H. Montrezor, L.G.D. Benevenuto, B.F. Antunes, A.C. Amaral, L.P. Novo, A.J.F.
762 Carvalho, E. Trovatti, The influence of chitosan, cellulose and alginate chemical
763 nature on mineral matrix formation, *Int J Polym Mater* **71** (2022) 875–885.
- 764 [58] E.M. Fernandes, R.A. Pires, J.F. Mano, R.L. Reis, Bionanocomposites from
765 lignocellulosic resources: Properties, applications and future trends for their use in
766 the biomedical field, *Prog Polym Sci* **38** (2013) 1415–1441.
- 767 [59] I.K. Susheel Kalia, B. S. Kaith, Cellulose Fibers: Bio- and Nano-Polymer
768 Composites, Springer Berlin Heidelberg, 2011.
- 769 [60] R. Lucas, Ueber das Zeitgesetz des kapillaren Aufstiegs von Flüssigkeiten,
770 *Kolloid-Zeitschrift* **23** (1918) 15–22.
- 771 [61] W. Gardner, Note on the dynamics of capillary flow, *Physical Review* **18** (1921)
772 206–209.
- 773 [62] A. Hamraoui, K. Thuresson, T. Nylander, V. Yaminsky, Can a dynamic contact
774 angle be understood in terms of a friction coefficient?, *J Colloid Interface Sci* **226**
775 (2000) 199–204.
- 776 [63] A. Hamraoui, T. Nylander, Analytical Approach for the Lucas–Washburn
777 Equation, *J Colloid Interface Sci* **250** (2002) 415–421.
- 778